Timescales of subduction initiation and evolution of subduction thermal regimes

Mathieu Soret, Guillaume Bonnet, Philippe Agard, K.P. Larson, J.M. Cottle, Benoît Dubacq, A.R.C. Kylander-Clark, M. Button, N. Rividi

Timescales of subduction initiation and evolution of subduction thermal regimes

M. Soret[1,2]*, G. Bonnet[3,4], P. Agard[4], K.P. Larson[1], J.M. Cottle[3], B. Dubacq[4], A.R.C. Kylander-Clark[3], M. Button[5], N. Rividi[6].

[1]Earth and Environmental Sciences, University of British Columbia Okanagan, 3247 University Way, Kelowna, British Columbia, V1V 1V7, Canada.

[2]Institut des Sciences de la Terre d'Orléans (ISTO), UMR 7327, CNRS–BRGM, Université d'Orléans, 45071, Orléans, France

[3]Department of Earth Science, University of California, Santa Barbara, Santa Barbara, CA93106, USA.

[4]Sorbonne Université, CNRS-INSU, Institut des Sciences de la Terre Paris, ISTeP UMR 7193, 75005 Paris, France.

[5]Fipke Laboratory for Trace Element Research, University of British Columbia Okanagan, Kelowna, BC, V1V 1V7, Canada.

[6]Sorbonne Université, OSU Ecce Terra, CAMPARIS laboratory, 75005 Paris, France.

**Corresponding author: math.soret@gmail.com*

Contact details

M. Soret: math.soret@gmail.com ORCID: 0000-0002-3000-805X

G. Bonnet: gbonnet01@gmail.com ORCID: 0000-0002-4128-9037

P. Agard: philippe.agard@sorbonne-universite.fr ORCID: 0000-0002-9413-5090

K.P. Larson: kyle.larson@ubc.ca ORCID: 0000-0002-1850-1896

J.M. Cottle: cottle@geol.ucsb.edu ORCID: 0000-0002-3966-6315

B. Dubacq: benoit.dubacq@sorbonne-universite.fr ORCID: 0000-0001-6927-0656

A.R.C. Kylander-Clark: kylander@geol.ucsb.edu ORCID: 0000-0002-4034-644X

M. Button: mark.button@ubc.ca ORCID: 0000-0002-9101-1682

N. Rividi: nicolas.rividi@sorbonne-universite.fr

Highlights

- Titanite and monazite in metamorphic soles record subduction initiation dynamics
- Initiation of the Neotethys subduction (Oman-UAE) was tectonically-induced prior to 102-100 Ma
- Subduction first stagnated for 5-10 Myr at warm conditions (15-20°C/km)
- Subduction evolved into a faster and colder self-sustained regime after 96-95 Ma

Abstract

Subduction zones are first-order features of plate tectonics on Earth, yet the mechanisms by which subduction initiates remain enigmatic and controversial. Here, we reappraise the timing of metamorphism of the rock units first detached from the leading edge of the downgoing slab during initiation of the Neotethys subduction, now preserved in the metamorphic sole of the Semail ophiolite (Oman–United Arab Emirates). Using petrochronology and phase equilibrium modeling, we demonstrate that subduction initiated prior to 102-100 Ma at a slow rate (< 1 cm/yr). Subduction stagnated at relatively warm conditions (15–20°C/km) for > 5 Myr before evolving into a faster (≥ 2–5 cm/yr) and colder (~7°C/km) self-sustained regime. Subduction acceleration (i.e. "unlocking" stage) triggered the onset of slab retreat, large-scale corner flow and fast ocean spreading in the overriding plate at 96–95 Ma, through the progressive change of thermo-mechanical structure of the plate interface. This study reconciles conflicting analogue and numerical subduction initiation models, shedding light on the thermal, mechanical and kinematic complexity of subduction initiation.

Keywords

- Petrochronology
- Metamorphic sole
- Semail ophiolite
- Subduction initiation
- Thermal evolution

1. Introduction

Subduction is one of the main facilitators of plate tectonics and yet the mechanisms responsible for subduction initiation are controversial (Stern and Gerya, 2017). How plate-scale mechanics and kinematics allow subduction to progress and reach steady-state remains unclear (Agard et al., 2018; Anczkiewicz et al., 2004; Crameri et al., 2020; Gurnis et al., 2004; Holt and Condit, 2021). Direct geological records of subduction initiation are limited to metamorphic soles, which correspond to thin sheets of deformed and metamorphosed oceanic crust. Metamorphic soles underlie the mantle section of most ophiolitic complexes (e.g., Oman–United Arab Emirates, Turkey, Newfoundland; Wakabayashi and Dilek, 2003) and are interpreted as remnants of the tip of the downgoing slab metamorphosed and deformed at high temperature along the nascent subduction interface (Agard et al., 2016; Wakabayashi and Dilek, 2003; Fig. 1a). These 10–500 m thick soles show remarkably similar characteristics worldwide (Agard et al., 2016), with a downward decrease in metamorphic grade from granulite/amphibolite facies to greenschist facies and an increase in the proportion of metasediments. This inverted sequence attests to sequential removal of crustal slices from the slab (e.g. HTa and HTb in Fig. 1a) and accretion to the base of the ophiolite during subduction initiation (Gnos, 1998; Soret et al., 2017). Metamorphic soles therefore mark episodes of viscous coupling along the plate interface before strain localization – and hence subduction – is achieved (Fig. 1b). With cooling of the interface, the depth of viscous coupling between the downgoing plate ('slab') and the overlying mantle is expected to migrate downwards (Agard et al., 2020) to 80–100 km in mature subduction zones (Syracuse et al., 2010). This deepening of viscous coupling enables subduction initiation (a mechanism coined "slabitization" by Agard et al., 2020) and may trigger and control mantle upwelling and counterflow in the upper plate ophiolite (Fig. 1b).

93 Constraining the relative timing and duration of these coupling events is essential to
94 understanding both subduction initiation and the birth of ophiolites (Fig. 1a). Two conflicting
95 end-member models for subduction initiation have been proposed (Stern, 2004): (1) "induced"
96 or "far-field forced" subduction initiation, in which subduction nucleates in response to a
97 regional change in plate dynamics (Agard et al., 2007; Duretz et al., 2016; Gurnis et al., 2004;
98 Hall et al., 2003; Moores, 1982; Rodriguez et al., 2021; Van Hinsbergen et al., 2015), (2)
99 "spontaneous" subduction initiation, in which subduction ensues from the gravitational sinking
100 of dense lithosphere in the absence of significant plate convergence (Arculus et al., 2015;
101 Dymkova and Gerya, 2013; Stern, 2004). Regardless of the model, the upper plate ophiolite is
102 thought to form by upwelling of supra-subduction mantle once subduction has initiated (e.g.,
103 Rioux et al., 2016), and numerical and analogue experiments (Duretz et al., 2016; Stern and
104 Gerya, 2017) only reproduce subduction initiation with fast-paced convergence (> cm/yr) along
105 a pre-existing lithospheric-scale weak zone.
106
107 $^{40}Ar/^{39}Ar$ and U–Pb geochronology of metamorphic soles and associated ophiolites (Garber et
108 al., 2020; Gnos and Peters, 1993; Hacker, 1994; Hacker et al., 1996; Rioux et al., 2021b, 2016,
109 2013; Soret et al., 2016) commonly advocate for synchronous slab burial and ocean spreading
110 in the upper plate, as predicted by the spontaneous subduction initiation model (Stern, 2004).
111 However, garnet Lu–Hf dating of the highest-grade sole unit (accreted first, HTa on Fig. 1a, b)
112 in the Semail and Turkish exposures has recently revealed burial to granulite facies (~850°C)
113 ~8 Myr earlier than previously estimated, i.e. 103–104 Ma (Guilmette et al., 2018; Pourteau et
114 al., 2018) instead of 96–95 Ma (Gnos and Peters, 1993; Hacker, 1994; Hacker et al., 1996;
115 Rioux et al., 2016). U-Pb dating of zircon rims included in garnet from a lower-grade unit (HTb;
116 T~650°C) confirms that prograde metamorphism started ≥ 98.7 ± 1.7 Ma (Garber et al., 2020).
117 Dates from the cores of the same zircon grains (107–102 ± 2 Ma), though coeval within

uncertainty with the garnet dates from the HTa unit (Guilmette et al., 2018), were interpreted as detrital (Garber et al., 2020).

These few garnet and zircon dates from the HTa and HTb units indicate that subduction initiated before the formation of the associated supra-subduction zone ophiolite (96–95 Ma; Rioux et al., 2016), supporting the view that ophiolite-sole couples record far-field forcing before upper plate extension (Agard et al., 2007; Guilmette et al., 2018; Rodriguez et al., 2021; Van Hinsbergen et al., 2015) rather than spontaneous subduction initiation. Yet, these older dates have not yet been robustly ascribed to specific P–T conditions and as such provide only little information on the timescale and rate of slab sinking during subduction initiation (Fig. 1b).

This study uses thermodynamic modeling tied to *in situ* titanite and monazite dating of the sub-units of the Semail metamorphic sole (Oman–UAE) to precisely quantify the temporal record of their burial, accretion and exhumation. This new dataset provides direct information on i) the onset, duration and rate of subduction initiation, ii) thermo-mechanical processes along the plate interface and iii) the link between these processes and the supra-subduction ophiolite formation.

2. The Semail metamorphic sole units

The Semail metamorphic sole comprises a dominantly mafic, high-temperature (HT) unit thrust onto a mainly metasedimentary low-temperature (LT) unit (Fig. 2a, b; Gnos, 1998). The HT sole itself consists of two tectonic slices juxtaposed sequentially, HTa then HTb (Soret et al., 2017). The latter is capped by a meter-thick garnet-rich metasedimentary layer. Specimens were collected from the Khubakhib and Sumeini half-windows (UAE and Oman, respectively; Fig.

142 2a, b), where the structure of the Semail metamorphic sole is well preserved (Gnos and Peters,
143 1993; Soret et al., 2017).
144
145 **2.1. Mineralogy and P-T conditions of formation**
146 The strongly foliated granulite-facies metabasalts of HTa preserve a prograde to peak
147 metamorphic assemblage of garnet, clinopyroxene, amphibole and minor plagioclase (Cowan
148 et al., 2014; Gnos, 1998; Guilmette et al., 2018; Soret et al., 2019a, 2017), despite partial
149 overprinting at amphibolite facies conditions. Titanite occurs as euhedral to subhedral
150 inclusions in both prograde and peak phases (i.e. garnet and clinopyroxene porphyroclasts; Ti-
151 rich amphibole; Fig 3a-c), forming locally rotated inclusion trails (Gnos, 1998). Rutile and
152 zircon occur as small inclusions (1–10 μm) in garnet and titanite (Fig. 3b).
153
154 Amphibolite-facies metabasalts of HTb mainly consist of amphibole and plagioclase with
155 minor biotite and either clinopyroxene or chemically zoned garnet (Garber et al., 2020; Soret
156 et al., 2019a, 2017). Titanite forms euhedral to subhedral grains closely associated with both
157 amphibole and plagioclase, either as inclusions or along boundaries (Fig. 3e-f). Rutile and
158 zircon form small inclusions (1–30 μm) in titanite and amphibole (Fig. 3e). In the presence of
159 garnet, ilmenite is observed instead of titanite (Soret et al., 2017).
160
161 The sheared metasedimentary layer at the top of HTb is dominated by quartz, garnet, muscovite
162 and plagioclase. Garnet cores host quartz and ilmenite inclusions (Fig. 3g). Garnet mantles
163 contain minute zircon grains as well as abundant polycrystalline inclusions with a negative
164 crystal shape (Fig. 3g-i), indicating peritectic growth reaction (Cesare et al., 2009; Dubacq et
165 al., 2019). Garnet rims are thin (≤ 150 μm) and typically inclusion-free, save for minute

166 monazite and zircon (1–10 μm). Large monazite (50–100 μm; Fig. 3j, k) occurs in the rock
167 matrix where it is rimmed by a syn-kinematic assemblage of epidote, allanite and apatite.
168
169 Peak P–T conditions for the HTa, HTb and LT units of the sole are estimated at 850 ± 50°C
170 and 1.0 ± 0.1 GPa, 725 ± 50°C and 0.8 ± 0.1 GPa, and 530 ± 50°C and 0.5 ± 0.1 GPa,
171 respectively (Soret et al., 2017). For HTa, no significant petrological/P-T variations have been
172 found along strike, despite being separated by hundreds of kilometers beneath the ophiolite
173 (Khubakhib, Sumeini and Wadi Tayin areas; Soret et al., 2017). The P–T conditions for HTb
174 are less precisely known (Soret et al., 2017; Garber et al., 2020) and therefore reassessed here
175 (see section 4.1).
176
177 **2.2. Existing geochronology**
178 Zircon U–Pb dating of melt segregations in HTa indicates melt crystallization and incipient
179 cooling by 96.2–94.5 Ma (Guilmette et al., 2018; Rioux et al., 2016). Hornblende $^{40}Ar/^{39}Ar$
180 dating indicates cooling below 500–550°C (Ar diffusion closure temperature) shortly
181 thereafter, between 95.7 and 92.6 Ma (Gnos and Peters, 1993; Hacker et al., 1996). A subset of
182 four titanite grains in HTa yielded a single $^{206}Pb/^{238}U$ age of 95.6 ± 0.3 Ma, which was
183 interpreted as a cooling age below 600–650°C (Guilmette et al., 2018). Finally, titanite and
184 monazite U–Pb dating combined with garnet Lu–Hf dating in a lower grade unit (peak
185 T~650°C) indicate prograde to peak growth age from 98.7 ± 1.7 Ma to 93.0 ± 0.5 Ma (Garber
186 et al., 2020). A single titanite U–Pb date of 92.2 ± 1.8 Ma is interpreted to record the initial
187 cooling of this unit (Garber et al., 2020). Fast cooling of both HTa and HTb sole units shortly
188 after reaching peak conditions is further supported by the preservation of prograde chemical
189 zoning in garnet (Garber et al., 2020; Guilmette et al., 2018; Soret et al., 2019a, 2017).
190

3. Results

A detailed description of the different methods used in this study is provided in the supplementary materials.

3.1. Phase equilibrium modeling

The P–T evolutions of the two garnet-bearing HTb specimens (metasediment: SE13-123L; metabasalt: SE16-26) determined through forward thermodynamic modeling (Perple_X software version 6.8.6; Connolly, 2009; Connolly and Kerrick, 1987) are shown in Figure 4a-c. The P–T history of the HTa unit has previously been estimated by Soret et al. (2017). Mineral abbreviations throughout the text, figures, tables and supplementary information are after Whitney and Evans (2010).

The pseudosections (Fig. 4a-b) for mafic composition from the HTb unit (Tab. SM3) have been modeled in the NCKFMASHT system using the internally consistent thermodynamic dataset (hp62ver.dat) of Holland and Powell (2011). The H_2O value was set to 1.0 wt.% after calculating a T-X(H_2O) diagram (Fig. 3a) with a water content ranging from 0.5 wt.% to 2.0 wt.% (i.e., excess water) at a pressure of 0.75 GPa consistent with the estimates from the amphibole-plagioclase thermo-barometry (~0.75 GPa and 750°C; inset of Fig. 3a; Holland and Blundy, 1994; Molina et al., 2015). The H_2O value is similar to that reported in the literature for similar metamorphic sole amphibolites (Mont Albert, Andaman, Oman-UAE; Dubacq et al., 2019; Plunder et al., 2020; Soret et al., 2017). The pseudosection (Fig. 4c) for the felsic composition (Tab. SM3) has been modelled in the CKFMASH system using the internally consistent thermodynamic dataset (hp02ver.dat) of Holland and Powell (1998). The H_2O content was calculated to be in excess at subsolidus conditions and with a water-saturated solidus at 0.8 GPa. The P–T estimates were determined based on the observed mineral assemblage and the isopleth compositions of garnet (Fig. 4b, c) for both specimens because

most of the plagioclase, biotite and muscovite (re-)crystallized during retrograde metamorphism (Soret et al., 2017).

Peak P–T conditions inferred for the Grt + Amp + Pl + Bt + Ilm ± Qz assemblage of the garnet-bearing amphibolite (SE16-26, Sumeini; Fig. 4a, b) lie at sub-solidus conditions of 725 ± 25°C and 0.77 ± 0.03 GPa. In addition to the calculated garnet rim composition ($Alm_{65-66}Prp_{17-18}Grs_{17}$), calculated modes ($Grt_{10}Amp_{35}Pl_{38}Bt_{10}Ilm_{2.5}$) and plagioclase composition (An_{41}) are in close agreement with those observed in the specimen (Soret et al., 2017). Garnet core isopleths converge at 625 ± 20°C and 0.70 ± 0.02 GPa in the same stability field.

Peak P–T conditions for the garnet-bearing metasediment (SE13-123L, Khubakhib; Fig. 4c) lie above the wet solidus for felsic rocks, at 750 ± 10°C and 0.76 ± 0.02 GPa, in the field of Grt + Bt + Qz + Sil + Pl + WM + melt. These conditions were determined using isopleth intersections for the peritectic garnet mantle ($Alm_{69-71}Prp_{18-19}Grs_{12-13}$). The composition of the quartz-rich garnet core ($Alm_{67-68}Prp_{13-14}Grs_{18-19}$) indicates a prograde, near-isobaric evolution from 610 ± 10°C and 0.72 ± 0.2 GPa. The thin inclusion-free garnet rim ($Alm_{76-77}Prp_{12}Grs_{11}$) further indicates sub-solidus re-equilibration during retrograde P–T conditions at 660 ± 20°C and 0.61 ± 0.03 GPa, in the white mica stability field. Considering the low proportion of sillimanite (< 9 vol%) expected along the PT path, its absence in the specimen could be explained by the extensive LT retrogression (Fig. 3g) and/or by reaction overstepping due to garnet nucleation (Spear and Pattison, 2017).

3.2. *In situ* titanite petrochronology

In situ U–Th/Pb and trace-element analyses of titanite and monazite (see section 3.3) were carried out on five HTa specimens and five HTb specimens (Fig. SM2, SM3) using the LASS

241 facility at the University of California, Santa Barbara (USA). Data reduction for U–Th/Pb,
242 including corrections for baseline, instrumental drift, mass bias, down-hole fractionation were
243 carried out using Iolite v. 2.5 (Paton et al., 2011), and error correlations were recalculated after
244 Schmitz and Schoene (2007). Methods used in this study follow those outlined by Kylander-
245 Clark et al. (2013), with modifications presented by McKinney et al. (2015).
246
247 Rutile and zircon, though present in all specimens, proved too small (≤ 20 μm) to be analyzed.
248 Different titanite age populations within each specimen in both HTa and HTb units were
249 distinguished based on their textural position and Rare Earth elements (REE) contents (Fig. 5).
250 Titanite ages were calculated for all titanite populations. They correspond to ^{207}Pb-corrected
251 (following Stacey and Kramers, 1975) ^{206}Pb/^{238}U weighted means, and they ranged between
252 94.7 and 100 Ma with MSWD between 0.9 and 2.7 (Tab. 1).
253
254 *3.2.1. The HTa metamorphic sole unit*
255 In SE11-23 (Sumeini), titanite grains are included in the core (G1) and the rim (G2) of a garnet
256 porphyroclast (Fig. 3c, 5a). Both inclusion sets show a depletion in HREE, while G2 is enriched
257 in LREE and Zr compared to G1 (Fig. 5a-c). G1 grains yielded older date (99.5 ± 0.7 Ma; spot
258 analyses (n) = 27) than those found at the rim (G2; 97.2 ± 0.3 Ma, n = 42).
259
260 In SE14-31 (Sumeini), titanite grains are either included at the core of a cm-scale garnet and a
261 mm-scale clinopyroxene or in the matrix. Five titanite populations were distinguished based on
262 variations in the textural position and REE concentrations (Fig. 5a, 5d-h). The first population
263 (G1) corresponds to inclusions in the garnet core. These titanite have flat REE patterns and
264 returned the oldest date (100.0 ± 2.0 Ma; n = 14). The second population (G2) comprises
265 inclusions in the core of both garnet and clinopyroxene. It exhibits a slight HREE depletion and

enrichment in Zr relative to G1, and yielded a date of 98.0 ± 0.9 Ma (n = 35). The third population (G3) also comprises inclusions in the core of garnet and clinopyroxene, but has a distinct REE pattern marked by an enrichment in LREE, a larger HREE depletion, and higher Zr concentrations than G2. G3 titanite yielded a date of 95.8 ± 0.5 Ma (n = 74). The fourth titanite population (G4) in this specimen consists of inclusions in the core of garnet and clinopyroxene together with titanite found in the matrix. These grains show a higher enrichment in LREE with a similar HREE depletion, and the highest Zr concentrations of any of the titanite populations in SE14-31. G4 titanite yielded a date of 95.9 ± 0.5 Ma (n = 93), which overlaps with that of G3 grains. The last population (G5) includes solely titanite grains from the matrix. The grains are characterized by a LREE content similar to G4 but with a significant enrichment in HREE. G5 titanite returned the youngest date in the specimen (94.9 ± 0.7 Ma; n = 35).

In SE13-123A (Khubakhib), titanite grains are included at the rim of three slightly zoned garnet porphyroclasts (Fig. 5a). These grains have a significant depletion in HREE relative to other REE (Fig. 5i), and yielded a date of 96.9 ± 0.4 Ma (n = 98). In SE13-123B (Khubakhib), titanite grains are found only in the matrix. They have high REE and Zr contents with a pattern marked by a slight depletion in HREE relative to LREE (Fig. 5j). The titanite in this specimen returned a date of 96.6 ± 0.9 Ma (n = 57). In SE13-123G (Khubakhib), titanite grains are included at the core of a cm-scale garnet (Fig. 5a). They display a REE pattern characterized by a large depletion in LREE relative to chondrites (Fig. 5k), and yielded a date of 99.6 ± 1.1 Ma (n = 33).

Titanite from the HTa unit has an average Zr content varying between 210 and 575 (± 50) ppm which is negatively correlated with the calculated ^{207}Pb-corrected ^{206}Pb/^{238}U mean dates (Fig. 5b-k; Tab. 1).

291 3.2.2. *The HTb metamorphic sole unit*

292 At Sumeini, titanite is texturally associated with amphibole and plagioclase in garnet-free rocks.
293 In all specimens, it shows a slight depletion in HREE relative to the LREE (Fig. 5l-r). Different
294 age populations within each specimen were distinguished based on variations in Zr and REE
295 concentrations. In SE14-16B (Fig. 5l-m), G1 titanite yielded a date of 97.2 ± 1.4 Ma (n = 15),
296 while G2 returned a date of 96.3 ± 0.8 Ma (n = 36). In SE14-17C (Fig. 5n-o), G1 gave a date
297 of 98.8 ± 1.1 Ma (n = 16) and G2 yielded a date of 97.0 ± 0.6 Ma (n = 31). In SE16-20 (Fig.
298 5p-q), G1 returned a date of 95.2 ± 1.3 Ma (n = 9), while G2 gave a date of 95.4 ± 0.8 Ma (n =
299 21). In SE16-11 (Fig. 5r), titanite grains are homogenous in composition and yielded a date of
300 94.7 ± 0.8 Ma (n = 23).
301
302 The different titanite populations from the HTb unit have an average Zr content varying
303 between 150 and 310 (± 25) ppm, with the highest concentration in the 96-95 Ma old population
304 (Fig. 5l-r; Tab. 1).
305
306 **3.3. *In situ* monazite petrochronology**
307 Eighteen monazite grains were dated in a metasediment sampled at the top of the HTb unit in
308 Khubakhib (Fig. 3j-k, SM3). All grains are located in the matrix. Monazite (1–10 μm)
309 inclusions in garnet were too small to get a reliable laser ablation signal. 190 spot analyses were
310 collected across 18 grains yielding most $^{208}Pb^*/^{232}Th$ dates between 102 Ma and 96 Ma (Fig.
311 6a-b).
312
313 Two monazite age populations are recognized based on their REE patterns (Fig. 6c-d). The first
314 population (G1) contains high Gd/Yb ratios (2180–2670) and low Y content (260–320 ppm).
315 Three grains (including the core of a zoned grain) were large enough for multiple analyses and

316 yielded weighted mean $^{208}Pb^*/^{232}Th$ dates of 99.2 ± 0.5 Ma (n = 27, SE13-123L2, Z1), 99.5 ±
317 0.6 Ma (n = 23, SE13-123L2, Z9) and 98.5 ± 0.4 Ma (n = 48, SE13-123L2, Z10 core). The
318 second population is characterized by low Gd/Yb ratios (20-40) and high Y content (6920-
319 21870 ppm). Analyses from four grains yielded weighted means of 97.6 ± 1.2 Ma (n = 7, SE13-
320 123L1, Z9), 96.6 ± 1.3 Ma (n = 7, SE13-123L2, Z3), 97.8 ± 1.1 Ma (n = 9, SE13-123L2, Z8)
321 and 97.5 ± 1.5 Ma (n = 6, SE13-123L2, Z10 rim).
322
323 **4. Discussion**
324 **4.1. P–T-t evolution of the Semail metamorphic sole**
325 Phase equilibrium modeling of both mafic and felsic lithologies helps refine the metamorphic
326 evolution of the HTb unit, particularly the pressure history. Peak P–T conditions of 750 ± 25°C
327 and 0.77 ± 0.03 GPa confirm the existence of a metamorphic gap with HTa (ΔT ~100°C, ΔP
328 ~0.2 GPa; Soret et al., 2017). The striking similarity of the clockwise P–T paths of HTb and
329 HTa (Fig. 7c) indicates a similar thermal history, characterized by a sub-isobaric temperature
330 increase (>100°C).
331
332 *In situ* titanite and monazite petrochronology allows assessment of the P–T–time paths of HTa
333 and HTb (Fig. 7c). The trace element zoning in titanite (Fig. SM4) rules out significant diffusive
334 homogenization subsequent to crystallization, as empirically demonstrated at temperatures of
335 850°C (Holder et al., 2019). Zirconium-in-titanite thermometry (Hayden et al., 2008) results
336 are, therefore, interpreted to reflect crystallization temperatures (Fig. 7a).
337
338 In HTa, the negative slope in REE of titanite inclusions in the core of chemically zoned garnet
339 and clinopyroxene porphyroclasts (Fig. 5) confirms they crystallized in equilibrium with garnet.
340 The Zr-poor titanite population (200–300 ppm) yields temperature estimates (750–800°C, at P

~0.7–1.0 GPa) similar to those predicted by phase equilibrium modeling for garnet nucleation at or near solidus conditions (Soret et al., 2017). Therefore, the weighted mean dates at 100–97 Ma are interpreted as the timing of garnet growth during increasing P-T conditions (time 1, t1; Fig. 7c). The flat REE pattern and the low Zr content displayed by the oldest age population (~100 Ma; G1 in SE14-31; Fig. 5c) could be interpreted as crystallization prior to garnet nucleation in that particular specimen. Moreover, temperatures of 815–840°C (at P ~1.0 GPa) are calculated from the Zr-rich titanite population (400-600 ppm). Because temperature estimates of this population overlap the calculated supra-solidus peak metamorphic conditions (Soret et al., 2017), the 96–95 Ma dates are interpreted as the age of peak P-T conditions (time 2, t2; Fig. 7c). The peritectic growth of this population is further supported by the enrichment in LREE (Fig. 5c,f,g,i,j) relatively to the oldest populations (100–98 Ma; Fig. 5b,d,e,k). It should also be noted that the earliest stages of garnet nucleation (> 100 Ma) recorded in some garnet cores were associated with the co-crystallization of rutile instead of titanite (Fig.5a; Soret et al., 2017), and given the relatively low closure temperature of rutile (Bonnet et al., *in press.*), could not be constrained in time

In HTb, the average Zr content in titanite is systematically lower than in HTa at a given age, consistent with cooler metamorphic conditions. The relatively flat REE pattern (Fig. 5) is also consistent with crystallization in a garnet-free environment. Zirconium-in-titanite thermometry yields a maximum temperature of 740–760°C (at P ~0.7 GPa), in agreement with peak metamorphic conditions estimated for this unit (Fig. 4a-c). Related weighted mean dates of 96-95 Ma are therefore interpreted as the time when HTb was accreted at peak conditions (t2; Fig. 7c). Older titanite grains (~99 Ma) contain less Zr on average, suggesting cooler temperatures ~725°C (at P ~0.7 GPa), consistent with crystallization along the prograde path near peak conditions and a lack of further re-equilibration of Zr.

366

367 Lead diffusivity in monazite is thought to be negligible up to temperatures of >800°C for grains
368 larger than 20 μm and over a period of ~10 Myr (Cherniak et al., 2004). Monazite dates in HTb
369 are, therefore, interpreted to represent crystallization ages. The combination of high (Gd/Yb)
370 ratios and low Y content in the (102–)100–98 Ma monazite (G1; Fig. 7b) is consistent with
371 prograde co-crystallization with xenotime and/or garnet. This is in contrast with low (Gd/Yb)
372 ratios and high Y content of 98-96 Ma monazite (G2; Fig. 7b), which are compatible with either
373 xenotime breakdown at amphibolite facies or garnet breakdown at supra-solidus conditions
374 along the prograde P-T path (Shrestha et al., 2019; Soret et al., 2019b; Spear and Pyle, 2010)
375 (t2; Fig. 7c). Because i) monazite tends to dissolve upon partial melting (Yakymchuk and
376 Brown, 2014), ii) phase equilibrium modeling does not predict any garnet breakdown along the
377 prograde P-T path, and iii) monazite appears to be partly dissolved at its edge (Fig. 3j, k), we
378 suggest that monazite records the prograde evolution of the HTb unit at amphibolite-facies from
379 (102–)100 Ma to 96 Ma, consistent with titanite petrochronology.
380

381 **4.2. Kinematics, mechanics and thermal structure of subduction initiation**

382 The results of this study indicate that the leading edge of the nascent slab preserved in the HTa
383 and HTb metamorphic sole units (Soret et al., 2017) reached peak T conditions at 96–95 Ma
384 (Fig. 4a), consistent with zircon U–Pb dates of 96.2–94.5 Ma for melt segregations in HTa
385 (Rioux et al., 2016). Therefore, both units appear to have been detached from the slab
386 synchronously with upper plate extension and associated spreading of the supra-subduction
387 zone ophiolite at 96.5–95.5 Ma.
388

389 In addition, the prograde record in titanite and monazite shows that amphibolite-facies
390 conditions of ~650–750°C were reached by (102–)100 Ma (Fig. 4a, 7c). These new data range

391 amongst the older set of dates published for the Semail metamorphic sole: the 104–103 Ma Lu–
392 Hf garnet dates for HTa (Guilmette et al., 2018) (Fig. 7a), and the 107–102 Ma U-Pb dates of
393 zircon cores found in a unit equivalent to HTb (Garber et al., 2020). In the latter study, the
394 zircon rims with low Th/U ratios (dated at 98.7–94.1 Ma) were reported to co-exist with Th-
395 rich monazite (dated at 97–89 Ma). The 107-102 Ma zircon cores with high Th/U ratios without
396 significant Eu anomalies may also have formed along the prograde P-T path prior to the
397 crystallization of monazite rather than representing detrital cores as interpreted.
398
399 Titanite U-Pb dates ranging from 100 to 96 Ma indicate that the Lu–Hf dates from the
400 chemically zoned garnet (Guilmette et al., 2018) may actually reflect continuous garnet growth
401 from > 104 Ma to 96 Ma. Significant isobaric heating is recorded in HTa during peak burial
402 garnet growth (>100°C; Fig. 7c), as reflected by phase equilibrium modeling (Soret et al.,
403 2017), increasing average Zr content (from 235 to 580 ppm; Fig. 4a), and steepening of the
404 REE pattern in titanite included in garnet. Consequently, HTa was not yet detached from the
405 slab at 104–103 Ma and was therefore not accreted to the upper plate at supra-solidus conditions
406 for 8 Myr, contrary to previous claims (Guilmette et al., 2018). Zoning in garnet (Garber et al.,
407 2020; Guilmette et al., 2018; Soret et al., 2017) and titanite (Fig. SM4) would also less likely
408 be preserved over such long periods (Cherniak, 2006). Furthermore, the Zr decrease in titanite
409 grains from the partly retrogressed matrix (SE14-31, G5) confirms the detachment of the HTa
410 metamorphic sole unit from the slab at 95 Ma, immediately after reaching peak P-T conditions.
411
412 This study quantifies the timescales for the transition from subduction nucleation to mature
413 subduction (“slabitization” stage; Agard et al., 2020; Fig. 7a) with emphasis on the evolution
414 of the force balance during convergence (Gurnis et al., 2004; Lallemand and Arcay, 2021;
415 Shuck et al., 2022).

The extensive U–Th/Pb dataset presented here confirms that subduction initiation predated upper plate extension at 96-95 Ma. It follows that subduction initiation was tectonically induced, probably by a major plate reorganization and plate acceleration event at 115-105 Ma (Agard et al., 2007; Matthews et al., 2015; Rodriguez et al., 2021; van Hinsbergen et al., 2021). From at least 102-100 Ma onwards (and probably as early 107–104 Ma) to 97-96 Ma, the future HTa and HTb soles were slowly subducted until peak burial (at 1.0 and 0.7–0.8 GPa, respectively) as shown by the warm excursion of the P-T path (Fig. 8c) and still attached to the slab. Petrochronology, therefore, reveals that subduction initiated at a slow rate < cm/yr, considering a 30° subduction dip angle, for 5–10 Myr (from t0 to t1; Fig. 8a, b). We refer to this period of slow subduction progress (i.e. rate < cm/yr; see also Anczkiewicz et al. (2004) for the Franciscan example) as "stagnation" (Fig. 8a, 9). The lack of subduction to greater depths is supported by the absence of pre-96 Ma subduction-related magmatism (Belgrano and Diamond, 2019; Rioux et al., 2021b, 2016).

This evolution can be explained by the combination of two resisting forces: the initial elastic flexure of the downgoing plate and the onset of viscous coupling at depth accompanying induced subduction initiation (Fig. 8c, 9). The nascent slab first encountered the serpentinized shallow mantle (at t0; Fig. 8a-c) followed by progressively drier and mechanically stronger mantle with increasing depth and temperature, which acted as a buttress (at t1, Fig. 8b; Agard et al., 2016): when the slab tip eventually reached a viscosity similar to that of the overlying metasomatized peridotites it became fully coupled with the warm mantle wedge (Agard et al., 2016). We relate garnet nucleation and growth in the metamorphic sole at ≥ 104–98 Ma (at T~650–750°C, ~30 km depth; Fig. 7c, 8c) to this stage of thermal and mechanical viscous coupling between the nascent plates (stagnation; Fig. 8a-c, 9).

Extensive slab dehydration along the coupled interface during stagnation (Fig. 8b, 9), as predicted by phase equilibrium modeling (Fig. 4), was critical for subduction progress. It promoted (i) viscous decoupling, through progressive hydration and viscosity decrease of the mantle wedge (Agard et al., 2016; Soret et al., 2019a) and (ii) slab pull, through slab densification (Hacker et al., 2003) induced by garnet-forming dehydration reactions (Fig. 8b). This combined thermal and mechanical evolution overcame mantle resistance, ending stagnation and triggered the fast "unlocking" of the nascent plate interface (~1 Ma; t2; Fig. 8a-c). Subduction unlocking coincided with a significant increase in the convergence rate (≥ 2–5 cm/yr; Fig. 9; Boudier et al., 1988; Duretz et al., 2016) and induced local, fast mantle upwelling and upper plate extension leading to spreading of a new lithosphere in ≤ 2 Myr (Rioux et al., 2021b, 2016) above the nascent subduction zone (Belgrano and Diamond, 2019; Godard et al., 2006; Haase et al., 2016). Associated heating (at t2; Fig. 7c, 8c) promoted slab melting (Fig. 8b), which explains the presence of *in situ* melts (Fig. 2h) and felsic intrusions in the mantle wedge (Haase et al., 2015; Rioux et al., 2021b, 2021a, 2016), both dated between 96 and 90 Ma. Mantle upwelling also facilitated the rapid exhumation of the metamorphic sole from 96–95 Ma onwards (t2; Figs. 8b, 9). Subduction rapidly evolved into a cold, self-sustained regime after the detachment of the last unit of metamorphic sole (LT sole; ~92 Ma; Fig. 8c) to reach thermal regimes similar to those modeled by van Keken et al. (2011) – characterized by evolved arc magmatism dated at 87 Ma (Bonnet et al., 2020).

This evolution reconciles otherwise conflicting geochronology and subduction initiation models in terms of mechanics, kinematics and thermal evolution. In particular, there is considerable agreement with dynamic models of present-day incipient subduction systems, in which the transition from forced to self-sustaining states is a 5–15 Myr-long continuous but

non-linear process requiring a critical amount of convergence and fluid released to overcome the initially large resisting forces (Gurnis et al., 2004; Lallemand and Arcay, 2021; Mao et al., 2017; Shuck et al., 2022). Although the critical convergence is a function of the age of the two plates, its average value of ~100 km in the dynamic models is consistent with that calculated for the Semail subduction system at the time metamorphic soles reached peak-P conditions (considering a 30° dip angle). Moreover, the interpretation that supra-subduction zone ophiolites form above a cooling plate interface during advanced stages of the subduction history ("unlocking" stage; Fig. 9) explains the occurrence of blueschist-facies metamorphism (~1.6 GPa and 590°C at 51–48 Ma; Tamblyn et al., 2019) following the earliest stages of supra-subduction zone magmatism (52–48 Ma; Ishizuka et al., 2011), as reported in the Izu–Bonin–Mariana forearc (i.e., the most-studied example of *in situ* subduction initiation).

Finally, P-T-t paths also show that the initial subduction thermal regime was colder than previously thought, at ~15–20°C/km (versus 25–30°C/km; t0, t1; Fig. 8c). Downward migration of viscous coupling and serpentinite stability, at approximately constant temperature, shifted subduction gradients towards colder values (t2; Fig. 8c). Our model thereby bridges the gap between subduction initiation and mature subduction and explains the transition from decoupling to full coupling (≥ 80 km) observed in active subduction zones across the same range of slab surface temperatures (t2; Fig. 8c, 9; Syracuse et al., 2010).

5. Conclusions

This petrochronology study of the Semail ophiolitic complex (Oman-UAE) provides information over the dynamics (mechanics, kinematics and thermal evolution) and duration of subduction initiation. It confirms that subduction of the Arabian Plate, which ultimately led to the obduction of the Semail ophiolite, was tectonically-induced by far-field forces prior to 100

Ma. It also shows that subduction started at a slow pace for ~10 Myr, with a closure rate < 1 cm/yr in increasingly warmer conditions, between ≥ 104–100 and 95 Ma ("stagnation" stage) and triggered incipient mantle convection and fast lithosphere formation at 96–95 Ma ("unlocking stage"), eventually leading to a faster (2–5 cm/yr) and colder self-sustained regime.

The rock record of the Semail ophiolite as read through high-resolution geochronology shows how thermo-mechanical changes of the plate interface allow subduction to proceed. Integrating these results into active subduction zone datasets reconciles conflicting models of subduction initiation and provides timescales for the evolution from subduction nucleation to (cold) mature subduction. It also provides a coherent scheme to understand inception of self-sustained subduction on Earth with modern-day plate tectonics.

ACKNOWLEDGMENTS

The authors are thankful to B.R. Hacker for constructive remarks on an earlier version of this manuscript. This research was financially supported by the E-FIRE project (NSF award OIA 1545903), the University of California Santa Barbara, a Marie Curie International Training Network (grant no. 604713) to P. Agard, a Natural Sciences and Engineering Research Council Discovery Grant (RGPIN-2016-06736) and Canada Foundation for Innovation John Evans Leadership Fund Award (31301) to K.P. Larson. M. Gurnis and F. Corfu are thanked for their constructive reviews and A. Webb is thanked for his editorial handling.

AUTHOR CONTRIBUTIONS

M.S. conceived the project and completed the petrological study. M.S and G.B. conducted and processed the U–Pb geochronological analyses, and are the principal authors of the manuscript. M.S, P.A. and B.D. carried out the field work. P.A. and K.L. co-supervised the project. J.C. and

A.K-C. helped in the acquisition of geochronological analyses. M.B and N.R. helped in the acquisition of the petrological data. All authors contributed to discussion of the results and to the manuscript.

COMPETING FINANCIAL INTERESTS STATEMENT

The authors declare no competing interests.

REFERENCES

Agard, P., Jolivet, L., Vrielynck, B., Burov, E., Monié, P., 2007. Plate acceleration: The obduction trigger? Earth Planet. Sci. Lett. 258, 428–441. https://doi.org/10.1016/j.epsl.2007.04.002

Agard, P., Plunder, A., Angiboust, S., Bonnet, G., Ruh, J., 2018. The subduction plate interface: Rock record and mechanical coupling (from long to short time scales). Lithos #pagerange#. https://doi.org/10.1016/j.lithos.2018.09.029

Agard, P., Prigent, C., Soret, M., Dubacq, B., Guillot, S., Deldicque, D., 2020. Slabitization:mechanisms controlling subduction development and viscous coupling. Earth-Science Rev.

Agard, P., Yamato, P., Soret, M., Prigent, C., Guillot, S., Plunder, A., Dubacq, B., Chauvet, A., Monié, P., 2016. Plate interface rheological switches during subduction infancy: control on slab penetration and metamorphic sole formation. Earth Planet. Sci. Lett. 451, 208–220. https://doi.org/10.1016/j.epsl.2016.06.054

Anczkiewicz, R., Platt, J.P., Thirlwall, M.F., Wakabayashi, J., 2004. Franciscan subduction off to a slow start: Evidence from high-precision Lu-Hf garnet ages on high grade-blocks. Earth Planet. Sci. Lett. 225, 147–161. https://doi.org/10.1016/j.epsl.2004.06.003

Arculus, R.J., Ishizuka, O., Bogus, K. a., Gurnis, M., Hickey-Vargas, R., Aljahdali, M.H.,

Bandini-Maeder, A.N., Barth, A.P., Brandl, P. a., Drab, L., do Monte Guerra, R., Hamada, M., Jiang, F., Kanayama, K., Kender, S., Kusano, Y., Li, H., Loudin, L.C., Maffione, M., Marsaglia, K.M., McCarthy, A., Meffre, S., Morris, A., Neuhaus, M., Savov, I.P., Sena, C., Tepley III, F.J., van der Land, C., Yogodzinski, G.M., Zhang, Z., 2015. A record of spontaneous subduction initiation in the Izu–Bonin–Mariana arc. Nat. Geosci. 8, 728–733. https://doi.org/10.1038/ngeo2515

Belgrano, T.M., Diamond, L.W., 2019. Subduction-zone contributions to axial volcanism in the Oman–U.A.E. ophiolite. Lithosphere 11, 399–411. https://doi.org/10.1130/L1045.1

Bonnet, G., Agard, P., Whitechurch, H., Fournier, M., Angiboust, S., Caron, B., Omrani, J., 2020. Fossil seamount in southeast Zagros records intraoceanic arc to back-arc transition: New constraints for the evolution of the Neotethys. Gondwana Res. 81, 423–444. https://doi.org/10.1016/j.gr.2019.10.019

Bonnet, G., Chopin, C., Locatelli, M., Kylander-clark, A.R.C., Hacker, B.R., n.d. Protracted subduction of the European hyperextended margin exposed across the Dora-Maira massif (Western Alps). Tectonics.

Boudier, F., Ceuleneer, G., Nicolas, A., 1988. Shear zones, thrusts and related magmatism in the Oman ophiolite: Initiation of thrusting on an oceanic ridge. Tectonophysics 151, 275–296. https://doi.org/10.1016/0040-1951(88)90249-1

Cesare, B., Ferrero, S., Salvioli-Mariani, E., Pedron, D., Cavallo, A., 2009. "Nanogranite" and glassy inclusions: The anatectic melt in migmatites and granulites. Geology 37, 627–630. https://doi.org/10.1130/G25759A.1

Cherniak, D.J., 2006. Zr diffusion in titanite. Contrib. to Mineral. Petrol. 152, 639–647. https://doi.org/10.1007/s00410-006-0133-0

Cherniak, D.J., Watson, E.B., Grove, M., Harrison, T.M., 2004. Pb diffusion in monazite : A combined RBS / SIMS study. Geochim. Cosmochim. Acta 68, 829–840.

https://doi.org/10.1016/j.gca.2003.07.012

Connolly, J.A.D., 2009. The geodynamic equation of state: What and how. Geochemistry, Geophys. Geosystems 10. https://doi.org/10.1029/2009GC002540

Connolly, J.A.D., Kerrick, D.M., 1987. An algorithm and computer program for calculating composition phase diagrams. Calphad 11, 1–55. https://doi.org/10.1016/0364-5916(87)90018-6

Cowan, R.J., Searle, M.P., Waters, D.J., 2014. Structure of the metamorphic sole to the Oman Ophiolite, Sumeini Window and Wadi Tayyin : implications for ophiolite obduction processes. Geol. Soc. London, Spec. Publ. 392, 155–175. https://doi.org/10.1144/SP392.8

Crameri, F., Magni, V., Domeier, M., Shephard, G.E., Chotalia, K., Cooper, G., Eakin, C.M., Grima, A.G., Gürer, D., Király, Á., Mulyukova, E., Peters, K., Robert, B., Thielmann, M., 2020. A transdisciplinary and community-driven database to unravel subduction zone initiation. Nat. Commun. 11, 1–14. https://doi.org/10.1038/s41467-020-17522-9

Dubacq, B., Soret, M., Jewison, E., Agard, P., 2019. Early subduction dynamics recorded by the metamorphic sole of the Mt. Albert ophiolitic complex (Gaspé Quebec). Lithos 334–335, 161–179. https://doi.org/10.1016/j.lithos.2019.03.019

Duretz, T., Agard, P., Yamato, P., Ducassou, C., Burov, E.B., Gerya, T. V, 2016. Thermo-mechanical modeling of the obduction process based on the Oman Ophiolite case. Gondwana Res. 32, 1–10. https://doi.org/10.1016/j.gr.2015.02.002

Dymkova, D., Gerya, T., 2013. Porous fluid flow enables oceanic subduction initiation on Earth. Geophys. Res. Lett. 40, 5671–5676. https://doi.org/10.1002/2013GL057798

Garber, J., Rioux, M., Kylander-Clark, A.R.C., Hacker, B.R., Vervoort, J.D., Searle, M.P., 2020. Petrochronology of Wadi Tayin Metamorphic Sole Metasediment, With Implications for the Thermal and Tectonic Evolution of the Samail Ophiolite

591 (Oman/UAE). Tectonics 39, TC006135. https://doi.org/10.1029/2020TC006135
592 Gnos, E., 1998. Peak Metamorphic Conditions of Garnet Amphibolites Beneath the Semail
593 Ophiolite: Implications for an Inverted Pressure Gradient. Int. Geol. Rev. 40, 281–304.
594 https://doi.org/10.1080/00206819809465210
595 Gnos, E., Peters, T., 1993. K-Ar ages of the metamorphic sole of the Semail Ophiolite:
596 implications for ophiolite cooling history. Contrib. to Mineral. Petrol. 113, 325–332.
597 https://doi.org/10.1007/BF00286925
598 Godard, M., Bosch, D., Einaudi, F., 2006. A MORB source for low-Ti magmatism in the
599 Semail ophiolite. Chem. Geol. 234, 58–78.
600 https://doi.org/10.1016/j.chemgeo.2006.04.005
601 Guilmette, C., Smit, M.A., Hinsbergen, D.J.J. Van, Gürer, D., Corfu, F., Charette, B.,
602 Maffione, M., Rabeau, O., Savard, D., 2018. Forced subduction initiation recorded in the
603 sole and crust of the Semail Ophiolite of Oman. Nat. Geosci.
604 https://doi.org/https://doi.org/10.1038/s41561-018-0209-2
605 Gurnis, M., Hall, C., Lavier, L., 2004. Evolving force balance during incipient subduction.
606 Geochemistry, Geophys. Geosystems 5, Q07001.
607 https://doi.org/10.1029/2003GC000681
608 Haase, K.M., Freund, S., Beier, C., Koepke, J., Erdmann, M., Hauff, F., 2016. Constraints on
609 the magmatic evolution of the oceanic crust from plagiogranite intrusions in the Oman
610 ophiolite. Contrib. to Mineral. Petrol. 171, 46. https://doi.org/10.1007/s00410-016-1261-
611 9
612 Haase, K.M., Freund, S., Koepke, J., Hauff, F., Erdmann, M., 2015. Melts of sediments in the
613 mantle wedge of the Oman ophiolite. Geology 43, 275–278.
614 https://doi.org/10.1130/G36451.1
615 Hacker, B.R., 1994. Rapid emplacement of young oceanic lithosphere: argon geochronology

616 of the Oman ophiolite. Science (80-.). 265, 1563–1565.
617 Hacker, B.R., Mosenfelder, J.L., Gnos, E., 1996. Rapid emplacement of the Oman ophiolite:
618 Thermal and geochronologic constraints. Tectonics 15, 1230–1247.
619 https://doi.org/10.1029/96TC01973
620 Hacker, B.R., Peacock, S.M., Abers, G.A., Holloway, S.D., 2003. Subduction factory 2 . Are
621 intermediate-depth earthquakes in subducting slabs linked to metamorphic dehydration
622 reactions ? J. Geophys. Res. 108, 2030. https://doi.org/10.1029/2001JB001129
623 Hall, C.E., Gurnis, M., Sdrolias, M., Lavier, L.L., Muller, R.D., 2003. Catastrophic initiation
624 of subduction following forced convergence across fracture zones. Earth Planet. Sci.
625 Lett. 212, 15–30. https://doi.org/10.1016/S0012-821X(03)00242-5
626 Hayden, L.A., Watson, E.B., Wark, D.A., 2008. A thermobarometer for sphene (titanite).
627 Contrib. to Mineral. Petrol. 155, 529–540. https://doi.org/10.1007/s00410-007-0256-y
628 Holder, R.M., Hacker, B.R., Seward, G.G.E., Kylander-Clark, A.R.C., 2019. Interpreting
629 titanite U–Pb dates and Zr thermobarometry in high-grade rocks: empirical constraints
630 on elemental diffusivities of Pb, Al, Fe, Zr, Nb, and Ce. Contrib. to Mineral. Petrol. 174,
631 1–19. https://doi.org/10.1007/s00410-019-1578-2
632 Holland, T., Blundy, J., 1994. Non-ideal interactions in calcic amphiboles and their bearing
633 on amphibole-plagioclase thermometry. Contrib. to Mineral. Petrol. 116, 433–447.
634 https://doi.org/10.1007/BF00310910
635 Holland, T.J.B., Powell, R., 2011. An improved and extended internally consistent
636 thermodynamic dataset for phases of petrological interest, involving a new equation of
637 state for solids. J. Metamorph. Geol. 29, 333–383. https://doi.org/10.1111/j.1525-
638 1314.2010.00923.x
639 Holland, T.J.B., Powell, R., 1998. An internally consistent thermodynamic data set for phases
640 of petrological interest. J. Metamorph. Geol. 16, 309–343.

https://doi.org/10.1111/j.1525-1314.1998.00140.x

Holt, A.F., Condit, C., 2021. Slab Temperature Evolution Over the Lifetime of a Subduction Zone A. Geochemistry Geophys. Geosystems. https://doi.org/10.1029/2020GC009476

Ishizuka, O., Tani, K., Reagan, M.K., Kanayama, K., Umino, S., Harigane, Y., Sakamoto, I., Miyajima, Y., Yuasa, M., Dunkley, D.J., 2011. The timescales of subduction initiation and subsequent evolution of an oceanic island arc. Earth Planet. Sci. Lett. 306, 229–240. https://doi.org/10.1016/j.epsl.2011.04.006

Kylander-Clark, A.R.C., Hacker, B.R., Cottle, J.M., 2013. Laser-ablation split-stream ICP petrochronology. Chem. Geol. 345, 99–112. https://doi.org/10.1016/j.chemgeo.2013.02.019

Lallemand, S., Arcay, D., 2021. Subduction initiation from the earliest stages to self-sustained subduction: Insights from the analysis of 70 Cenozoic sites. Earth-Science Rev. 221, 103779. https://doi.org/10.1016/j.earscirev.2021.103779

Mao, X., Gurnis, M., May, D.A., 2017. Subduction Initiation With Vertical Lithospheric Heterogeneities and New Fault Formation. Geophys. Monogr. Ser. 44, 11349–11356. https://doi.org/10.1002/2017GL075389

Matthews, K.J., Williams, S.E., Whittaker, J.M., Müller, R.D., Seton, M., Clarke, G.L., 2015. Geologic and kinematic constraints on Late Cretaceous to mid Eocene plate boundaries in the southwest Pacific. Earth-Science Rev. 140, 72–107. https://doi.org/10.1016/j.earscirev.2014.10.008

McKinney, T.S., Cottle, J.M., Lederer, G.W., 2015. Evaluating rare earth element (REE) mineralization mechanisms in Proterozoic Gneiss, Music Valley, California. Bull. Geol. Soc. Am. 127, 1135–1152. https://doi.org/10.1130/B31165.1

Molina, J.F., Moreno, J.A., Castro, A., Rodríguez, C., Fershtater, G.B., 2015. Calcic amphibole thermobarometry in metamorphic and igneous rocks: New calibrations based

666 on plagioclase/amphibole Al-Si partitioning and amphibole/liquid Mg partitioning.
667 Lithos 232, 286–305. https://doi.org/10.1016/j.lithos.2015.06.027
668 Moores, E.M., 1982. Origin and Emplacement of Ophiolites. Rev. Geophys. Sp. Phys. 20,
669 735–760.
670 Nicolas, A., Boudier, F., Ildefonse, B., Ball, E., 2000. Accretion of Oman and United Arab
671 Emirates ophiolite – Discussion of a new structural map. Mar. Geophyiscal Res. 21,
672 147–179. https://doi.org/10.1023/A:1026769727917
673 Paton, C., Hellstrom, J., Paul, B., Woodhead, J., Hergt, J., 2011. Iolite : Freeware for the
674 visualisation and processing of mass spectrometric data. J. Anal. At. Spectrom. 26,
675 2508–2518. https://doi.org/10.1039/c1ja10172b
676 Plunder, A., Bandyopadhyay, D., Ganerød, M., Advokaat, E.L., Ghosh, B., Bandopadhyay,
677 P., van Hinsbergen, D.J.J., 2020. History of Subduction Polarity Reversal During Arc -
678 Continent Collision: Constraints From the Andaman Ophiolite and its Metamorphic
679 Sole. Tectonics 39, 1–24. https://doi.org/10.1029/2019TC005762
680 Pourteau, A., Scherer, E.E., Schorn, S., Bast, R., Schmidt, A., Ebert, L., 2018. Thermal
681 evolution of an ancient subduction interface revealed by Lu–Hf garnet geochronology,
682 Halilbagi Complex (Anatolia). Geosci. Front. https://doi.org/10.1016/j.gsf.2018.03.004
683 Rioux, M., Benoit, M., Amri, I., Ceuleneer, G., Garber, J., Searle, M., Leal, K., 2021a. The
684 origin of felsic intrusions within the mantle section of the Samail ophiolite: Geochemical
685 evidence for three distinct mixing and fractionation trends. J. Geophys. Res. Solid Earth
686 n/a. https://doi.org/10.1029/2020JB020760
687 Rioux, M., Bowring, S., Kelemen, P., Gordon, S., Miller, R., Dudás, F., 2013. Tectonic
688 development of the Samail ophiolite: High-precision U-Pb zircon geochronology and
689 Sm-Nd isotopic constraints on crustal growth and emplacement. J. Geophys. Res. Solid
690 Earth 118, 2085–2101. https://doi.org/10.1002/jgrb.50139

691 Rioux, M., Garber, J., Bauer, A., Bowring, S., Searle, M., Kelemen, P., Hacker, B., 2016.
692 Synchronous formation of the metamorphic sole and igneous crust of the Semail
693 ophiolite: New constraints on the tectonic evolution during ophiolite formation from
694 high-precision U–Pb zircon geochronology. Earth Planet. Sci. Lett. 451, 185–195.
695 https://doi.org/10.1016/j.epsl.2016.06.051
696 Rioux, M., Garber, J., Searle, M.P., Kelemen, P., Miyashita, S., Adachi, Y., Bowring, S.,
697 2021b. High-precision U-Pb zircon dating of late magmatism in the Samail ophiolite: A
698 record of subduction initiation. J. Geophys. Res. Solid Earth n/a.
699 https://doi.org/10.1029/2020JB020758
700 Rodriguez, M., Arnould, M., Coltice, N., Soret, M., 2021. Long-term evolution of a plume-
701 induced subduction in the Neotethys realm. Earth Planet. Sci. Lett. 561, 116798.
702 https://doi.org/10.1016/j.epsl.2021.116798
703 Schmitz, M.D., Schoene, B., 2007. Derivation of isotope ratios, errors, and error correlations
704 for U-Pb geochronology using 205Pb-235U-(233U)-spiked isotope dilution thermal
705 ionization mass spectrometric data. Geochemistry Geophys. Geosystems 8, 1–20.
706 https://doi.org/10.1029/2006GC001492
707 Shrestha, S., Larson, K.P., Duesterhoeft, E., Soret, M., Cottle, J.M., 2019. Thermodynamic
708 modelling of phosphate minerals and its implications for the development of P-T-t
709 histories: A case study in garnet - monazite bearing metapelites. Lithos 334–335, 141–
710 160. https://doi.org/10.1016/j.lithos.2019.03.021
711 Shuck, B., Gulick, S.P.S., Van Avendonk, H.J.A., Gurnis, M., Sutherland, R., Stock, J.,
712 Hightower, E., 2022. Stress transition from horizontal to vertical forces during
713 subduction initiation. Nat. Geosci. 15, 149–155. https://doi.org/10.1038/s41561-021-
714 00880-4
715 Soret, M., Agard, P., Dubacq, B., Plunder, A., Yamato, P., 2017. Petrological evidence for

716 stepwise accretion of metamorphic soles during subduction infancy (Semail ophiolite,
717 Oman and UAE). J. Metamorph. Geol. 35, 1051–1080.
718 https://doi.org/10.1111/jmg.12267
719 Soret, M., Agard, P., Dubacq, B., Vitale-Brovarone, A., Monié, P., Chauvet, A., Whitechurch,
720 H., Villemant, B., 2016. Strain localization and fluid infiltration in the mantle wedge
721 during subduction initiation: Evidence from the base of the New Caledonia ophiolite.
722 Lithos 244, 1–19. https://doi.org/10.1016/j.lithos.2015.11.022
723 Soret, M., Agard, P., Ildefonse, B., Dubacq, B., Prigent, C., Rosenberg, C., Alpes, U.G.,
724 Savoie, U., Blanc, M., 2019a. Deformation mechanisms in mafic amphibolites and
725 granulites : record from the Semail metamorphic sole during subduction infancy. Solid
726 Earth 10, 1733–1755.
727 Soret, M., Larson, K.P., Cottle, J.M., Smit, M., Johnson, A., Shrestha, S., Ali, A., Faisal, S.,
728 2019b. Mesozoic to Cenozoic tectono-metamorphic history of the South Pamir – Hindu
729 Kush (Chitral, NW Pakistan): Insights from phase equilibria modelling , and garnet –
730 monazite petrochronology. J. Metamorph. Geol. 37, 633–666.
731 https://doi.org/10.1111/jmg.12479
732 Spear, F.S., Pattison, D.R.M., 2017. The implications of overstepping for metamorphic
733 assemblage diagrams (MADs). Chem. Geol. 457, 38–46.
734 https://doi.org/10.1016/j.chemgeo.2017.03.011
735 Spear, F.S., Pyle, J.M., 2010. Theoretical modeling of monazite growth in a low-Ca
736 metapelite. Chem. Geol. 273, 111–119. https://doi.org/10.1016/j.chemgeo.2010.02.016
737 Stern, R.J., 2004. Subduction initiation: spontaneous and induced. Earth Planet. Sci. Lett. 226,
738 275–292. https://doi.org/10.1016/j.epsl.2004.08.007
739 Stern, R.J., Gerya, T., 2017. Subduction initiation in nature and models: A review.
740 Tectonophysics. https://doi.org/10.1016/j.tecto.2017.10.014

741 Syracuse, E.M., van Keken, P.E., Abers, G.A., Suetsugu, D., Bina, C., Inoue, T., Wiens, D.,
742 Jellinek, M., 2010. The global range of subduction zone thermal models. Phys. Earth
743 Planet. Inter. 183, 73–90. https://doi.org/10.1016/j.pepi.2010.02.004
744 Tamblyn, R., Zack, T., Schmitt, A.K., Hand, M., Kelsey, D., Morrissey, L., Pabst, S., Savov,
745 I.P., 2019. Blueschist from the Mariana forearc records long-lived residence of material
746 in the subduction channel. Earth Planet. Sci. Lett. 519, 171–181.
747 https://doi.org/10.1016/j.epsl.2019.05.013
748 Van Hinsbergen, D.J.J., Peters, K., Maffione, M., Spakman, W., Guilmette, C., Thieulot, C.,
749 Plümper, O., Gürer, D., Brouwer, F.M., Aldanmaz, E., Kaymakci, N., 2015. Dynamics
750 of intraoceanic subduction initiation: 2. Suprasubduction zone ophiolite formation
751 andmetamorphic sole exhumation in context of absolute plate motions. Geochemistry,
752 Geophys. Geosystems 16, 1771–1785.
753 https://doi.org/10.1002/2015GC005746.Dynamics
754 van Hinsbergen, D.J.J., Steinberger, B., Guilmette, C., Maffione, M., Gürer, D., Peters, K.,
755 Plunder, A., Mcphee, P.J., Gaina, C., Advokaat, E.L., Vissers, R.L.M., Spakman, W.,
756 2021. A record of plume-induced plate rotation triggering subduction initiation. Nat.
757 Geosci. 14. https://doi.org/10.1038/s41561-021-00780-7
758 Wakabayashi, J., Dilek, Y., 2003. What constitutes “emplacement” of an ophiolite?:
759 Mechanisms and relationship to subduction initiation and formation of metamorphic
760 soles. Geol. Soc. London, Spec. Publ. 218, 427–447.
761 https://doi.org/10.1144/GSL.SP.2003.218.01.22
762 Whitney, D.L., Evans, B.W., 2010. Abbreviations for names of rock-forming minerals. Am.
763 Mineral. 95, 185–187. https://doi.org/10.2138/am.2010.3371
764 Yakymchuk, C., Brown, M., 2014. Behaviour of zircon and monazite during crustal melting.
765 J. Geol. Soc. London. 171, 465–479. https://doi.org/10.1144/jgs2013-115

766 **FIGURE CAPTIONS**

767 **Figure 1.** a) Conceptual model for the metamorphic sole and ophiolite formation during
768 subduction initiation (after Agard et al., 2016, and Guilmette et al., 2018). (b) Geodynamic
769 setting representing the evolution of oceanic subductions from birth to mature (cold) stage
770 ("slabitization stage"; after Agard et al., 2020). HTa, HTb and LT refer to the three main slivers
771 of metamorphic sole accreted to the upper plate during subduction (Soret et al., 2017).

772

773 **Figure 2.** (a) Simplified geological map of the Semail ophiolite, highlighting the outcrops of
774 metamorphic sole (modified after Nicolas et al., 2000); (b) Schematic log of the Semail
775 ophiolite showing the structural position of the specimens from Khubakhib (K) and Sumeini
776 (S) (modified after Soret et al., 2017). See Table 1 for details.

777

778 **Figure 3.** Petrography of the analyzed specimens. (a-f) Photographs of titanite in the mafic HTa
779 and HTb units of the Semail metamorphic sole; (g-k) Back-scattered images of a peritectic
780 garnet with nanogranitoid inclusions (g-i), and monazite (j,k) in a metasedimentary layer at the
781 top of HTb. Mineral abbreviations are after Whitney and Evans (2010).

782

783 **Figure 4.** Phase equilibria modelling for (a-b) a garnet-bearing (mafic) amphibolite (SE16-26,
784 Sumeini) and (b) a metasedimentary (felsic) rock (SE13-123L, Khubakhib) from HTb. (a) T–
785 X(H_2O) calculations for the mafic specimen at 0.75 GPa with water content comprised between
786 0.5 and 2.0 wt%. Inset shows the P–T estimates calculated from the amphibole-plagioclase
787 thermobarometer by Holland and Blundy (1994) and Molina et al. (2015). Arrows highlight the
788 inferred P–T path between garnet core and rim growth.

789

790 **Figure 5.** (a) Correlation between the titanite age populations and the garnet zoning in HTa.

The grey envelop and the red arrow outline the prograde zoning of garnet determined from different specimens of HTa (see Soret et al. (2017) for details). (b-r) Rare Earth element spider diagrams of titanite colored by Zr content (ppm) for each laser ablation spot. $^{206}Pb^*/^{238}U$ weighted mean dates are given ± 2 SE (see Fig. SM2 for details). Average Zr contents (ppm) are given ± 1 SE.

Figure 6. (a-b) $^{208}Pb^*/^{232}Th$ versus $^{206}Pb^*/^{238}U$ concordia plot of age data obtained from monazite in specimen SE13-123L (Khubakhib). All isotopic ratios were corrected for common Pb using the method detailed in the Method section. Two populations (G1 and G2) were distinguished based on their composition. (c-d) Monazite Rare Earth element spider diagrams for G1 and G2 (respectively) versus the Pb*/Th ages (± 2 SE).

Figure 7. Petrochronological results. (a) Zr content (ppm) and associated calculated temperatures (thermometer of Hayden et al., 2008) vs. $^{206}Pb^*/^{238}U$ dates (± 2 SE) of titanite from HTa (in red) and HTb (in blue). (b) Y content (ppm) (± 1 SE) vs. $^{208}Pb^*/^{232}Th$ dates weighted mean ages for monazite grains comprising more than 6 spot analyses (see Table 1 for details). (a-b) red and blue arrows highlight the prograde (P–)T–t paths of both metamorphic sole units during subduction infancy. Grey arrow outlines the retrograde history. The results are consistent with the thermodynamic modelling conducted in this study and by Soret et al. (2017). Major geodynamical events are outlined in grey for comparison. GPRE: global plate reorganization event. (c) Summary of P–T–t paths for each HTa and HTb. Ref.(1) : this study, (2) Guilmette et al. (2018), (3) Rioux et al. (2016), (4) Garber et al. (2020), (5) Hacker et al. 1996, (6) Matthews et al. (2015), (7) Rioux et al. (2021b).

Figure 8. Thermo-mechanical model for the early subduction dynamics. (a) Timeline

highlighting the major stages (t0, t1, t2) of the oceanic subduction, from birth to death. Three-stage mechanical (b) and thermal (c) evolution reconciling bridging the gap between subduction initiation dynamics and that of mature subduction zones. Markers 'a (HTa), b (HTb), c, d' are used to trace the slab evolution during the subduction history. Symbol (*) refers to ref. Agard et al. (2020).

Figure 9. Geodynamic setting representing the timescales of the Neotethys oceanic subduction next to Arabia. The evolution from subduction nucleation to (cold) mature subduction ("slabitization"; Agard et al., 2020) is first controlled by a stage of "stagnation" (104–97 Ma) followed by a stage of "unlocking" (96–92 Ma).

Table 1. U–Th/Pb dates and compositions of titanite and monazite from the Semail metamorphic sole.

FIGURE AND TABLE CAPTIONS FOR SUPPLEMENTARY INFORMATION

Document SM1. Detailed description of all the methods used in this study.

Figure SM1. Weighted mean ^{207}Pb-corrected ^{206}Pb/^{238}U dates of titanite. Weighted mean values are outlined by the black horizontal line, with the 95% confidence interval shown as a grey band. Spot analyses are plotted ± 2 SE, in red for HTa and in blue for HTb. Outliers rejected from the weighted mean calculations are shown as white bars.

Fig. SM2. BSE images of the dated titanite grains highlighting their textural positions and the laser ablation spot locations.

Figure SM3. Compositional map of Yttrium (number of counts) of monazite in specimen SE13-123L with LASS spot locations and related ^{208}Pb*/^{232}Th dates.

Figure SM4. Chemical map showing the Y and Zr zoning in a large titanite included in garnet

841 (SE13-123A).

842 **Table SM1.** Titanite U–Pb and Trace element analysis.

843 **Table SM2.** Monazite U–Th/Pb and Trace element analysis**.**

844 **Table SM3.** Bulk rock compositions (%wt) used for phase equilibrium modeling.

845

846

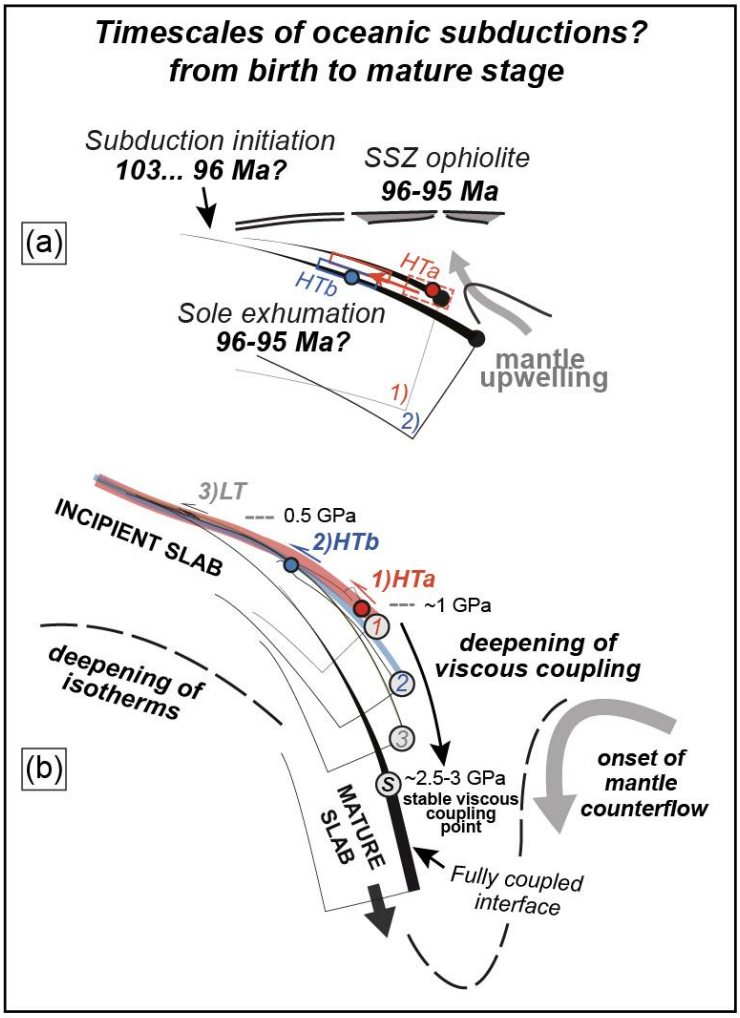

847 Figure 1

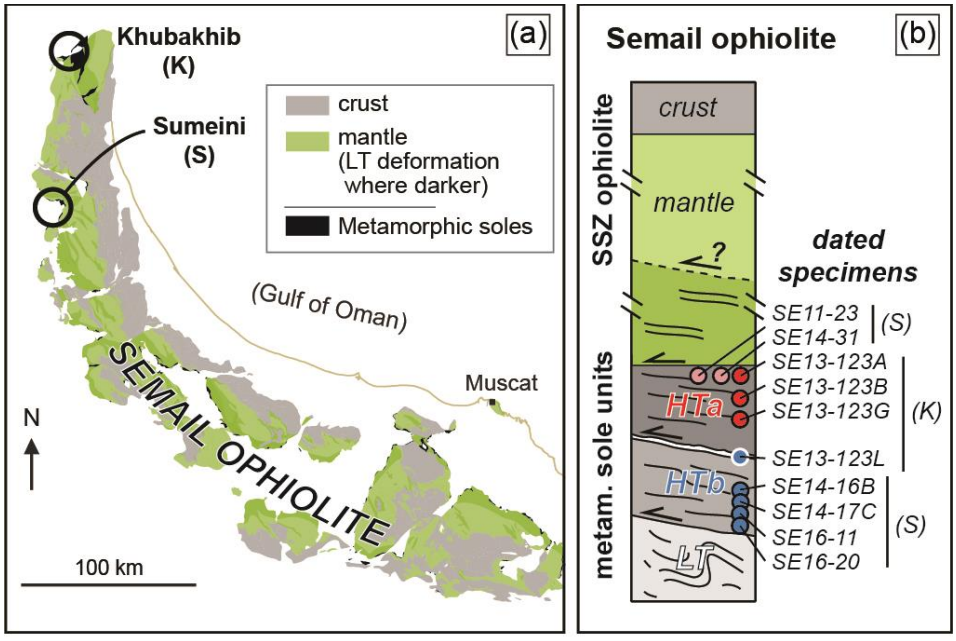

848 Figure 2

849

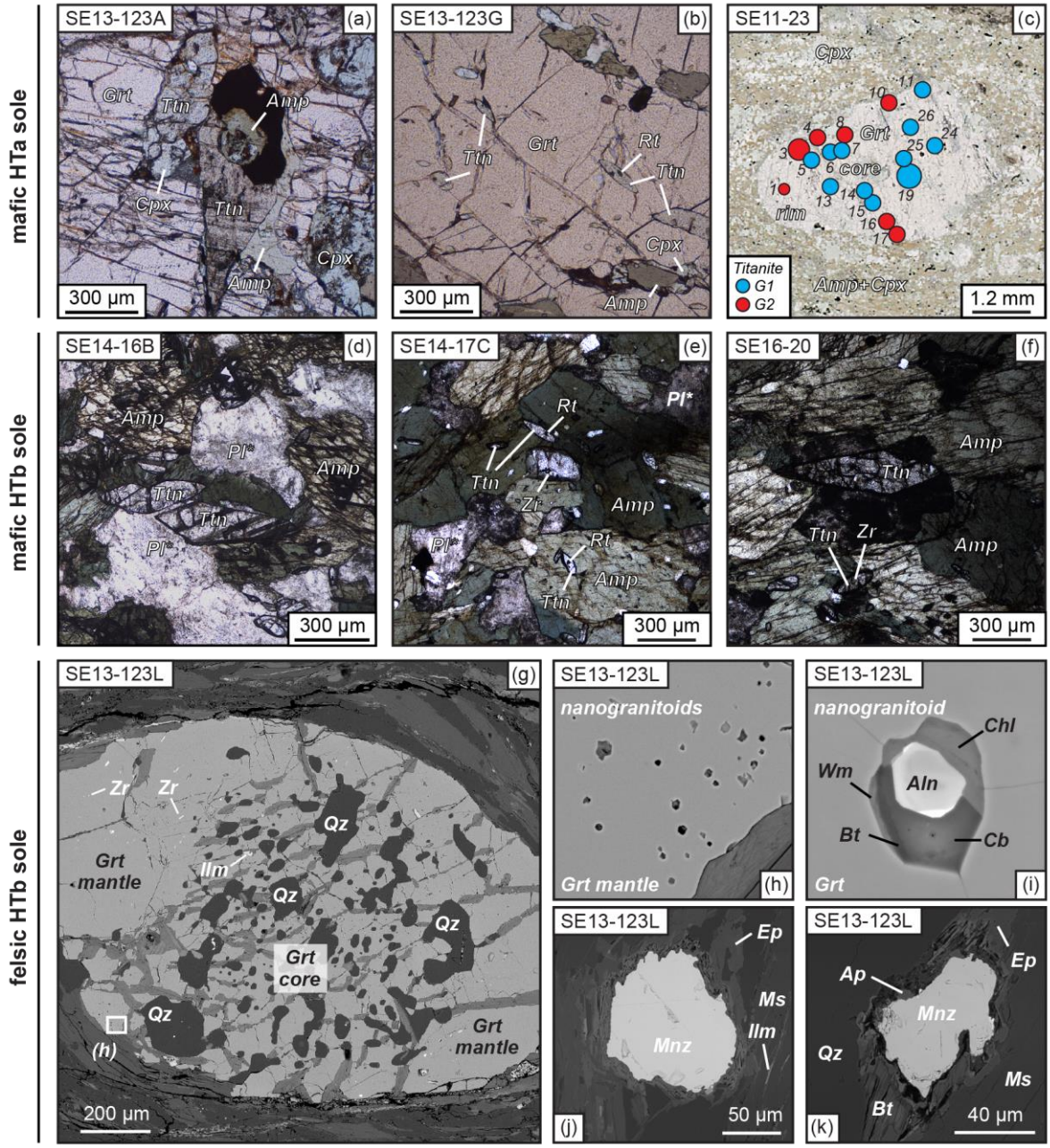
mafic HTa sole
SE13-123A
(a)
Grt
Ttn
Amp
Cpx
Ttn
Cpx
Amp
300 µm
SE13-123G
(b)
Ttn
Grt
Rt
Ttn
Cpx
Amp
300 µm
SE11-23
(c)
Cpx
Grt
core
rim
Titanite
G1
G2
Amp+Cpx
1.2 mm
mafic HTb sole
SE14-16B
(d)
Amp
Pl*
Amp
Ttn
Ttn
Pl*
300 µm
SE14-17C
(e)
Rt
Pl*
Ttn
Zr
Amp
Pl*
Rt
Amp
Ttn
300 µm
SE16-20
(f)
Amp
Ttn
Ttn
Zr
Amp
300 µm
felsic HTb sole
SE13-123L
(g)
Zr
Zr
Qz
Grt
mantle
Ilm
Qz
Qz
Grt
core
Qz
(h)
Grt
mantle
200 µm
SE13-123L
nanogranitoids
Grt mantle
(h)
SE13-123L
nanogranitoid
Chl
Wm
Aln
Bt
Cb
Grt
(i)
SE13-123L
Ep
Ms
Ilm
Mnz
(j)
50 µm
SE13-123L
Ep
Ap
Mnz
Qz
Ms
Bt
(k)
40 µm

Figure 3

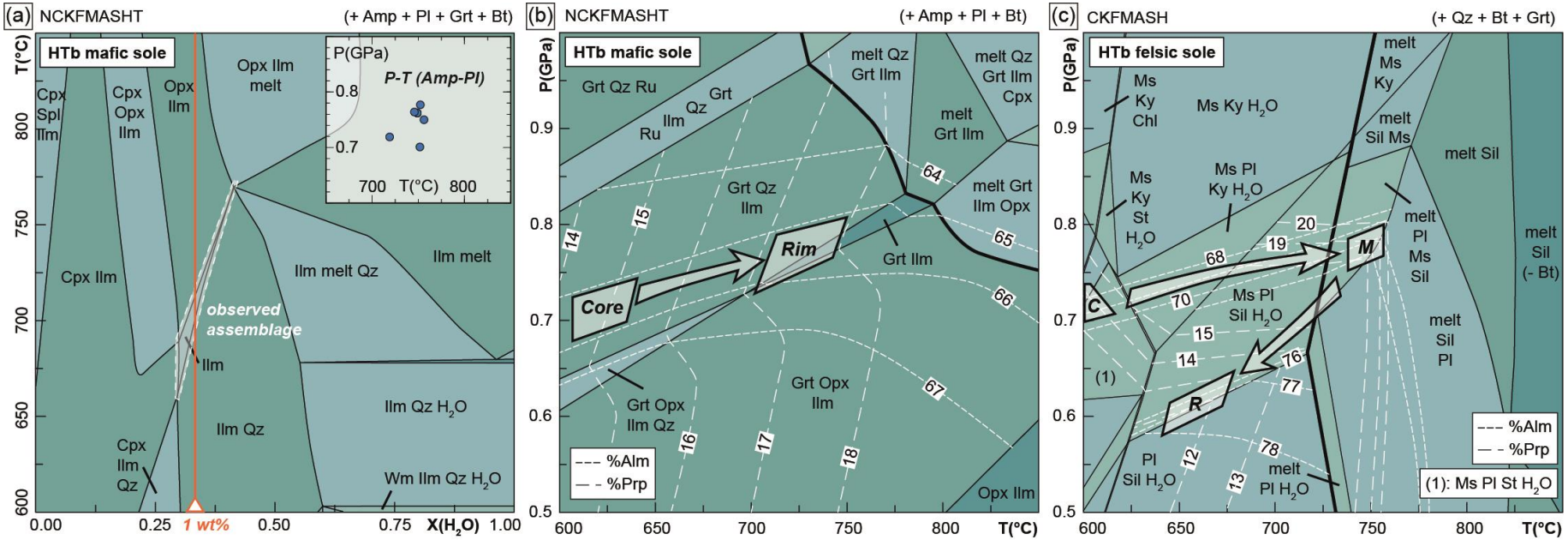
(a) NCKFMASHT
(+ Amp + Pl + Grt + Bt)
HTb mafic sole
T(°C)
P(GPa)
P-T (Amp-Pl)
0.8
0.7
700 T(°C) 800
Cpx Spl Ilm
Cpx Opx Ilm
Opx Ilm
Opx Ilm melt
Cpx Ilm
Ilm melt Qz
Ilm melt
observed assemblage
Ilm
Ilm Qz
Ilm Qz H2O
Cpx Ilm Qz
Wm Ilm Qz H2O
1 wt%
X(H2O)
(b) NCKFMASHT
(+ Amp + Pl + Bt)
HTb mafic sole
P(GPa)
Grt Qz Ru
Grt Qz Ilm Ru
melt Qz Grt Ilm
melt Qz Grt Ilm Cpx
melt Grt Ilm
melt Grt Ilm Opx
Grt Qz Ilm
Rim
Core
Grt Ilm
Grt Opx Ilm Qz
Grt Opx Ilm
Opx Ilm
--- %Alm
— - %Prp
T(°C)
(c) CKFMASH
(+ Qz + Bt + Grt)
HTb felsic sole
P(GPa)
Ms Ky Chl
Ms Ky H2O
melt Ms Ky
melt Sil Ms
melt Sil
Ms Ky St H2O
Ms Pl Ky H2O
melt Pl Ms Sil
melt Sil (- Bt)
M
C
Ms Pl Sil H2O
melt Sil Pl
(1)
R
Pl Sil H2O
melt Pl H2O
--- %Alm
— - %Prp
(1): Ms Pl St H2O
T(°C)

Figure 4

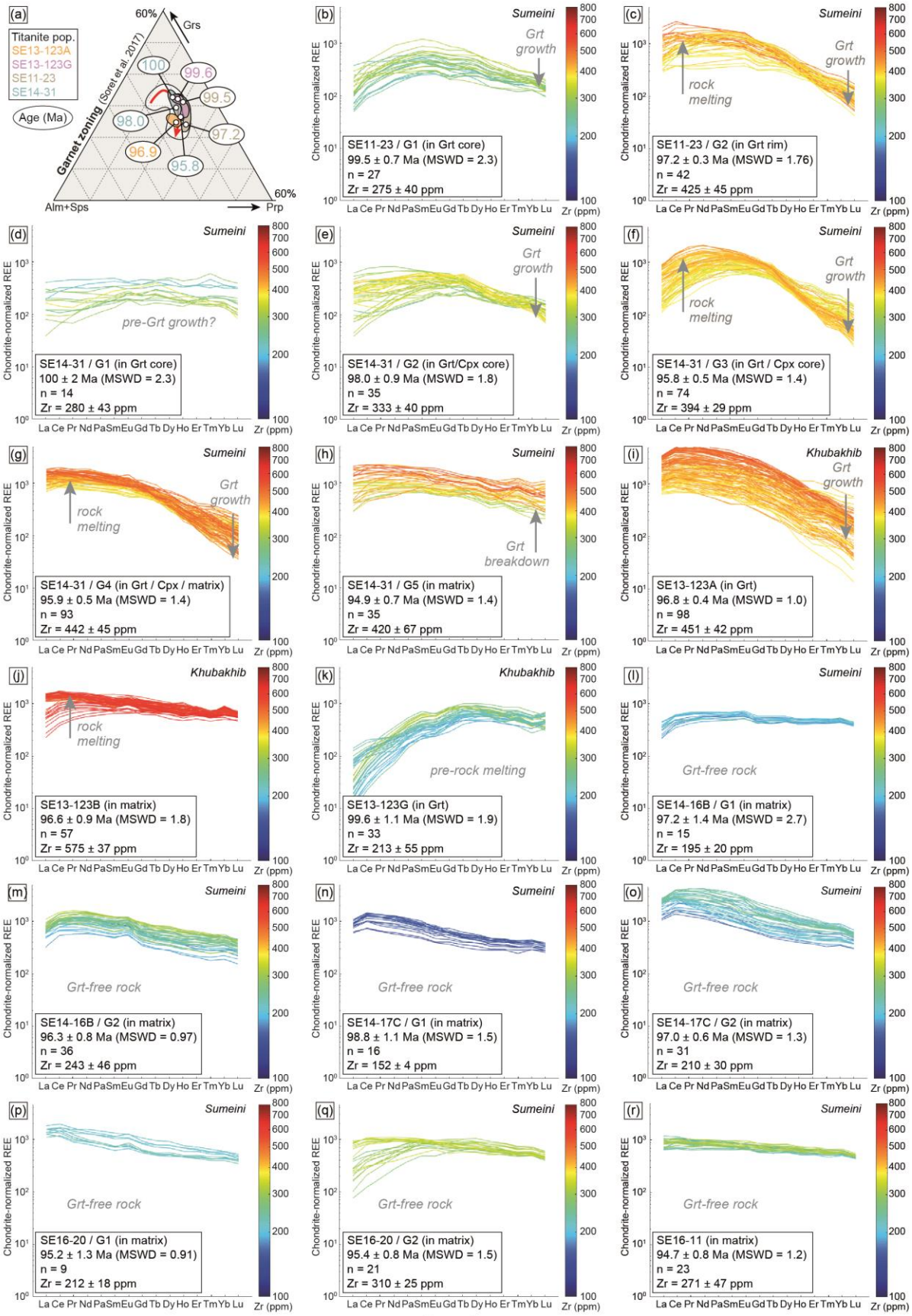
(a)
Titanite pop.
SE13-123A
SE13-123G
SE11-23
SE14-31
Age (Ma)
Garnet zoning (Soret et al. 2017)
60%
Grs
Alm+Sps
Prp
100
99.6
99.5
98.0
97.2
96.9
95.8
(b)
Sumeini
Grt growth
SE11-23 / G1 (in Grt core)
99.5 ± 0.7 Ma (MSWD = 2.3)
n = 27
Zr = 275 ± 40 ppm
(c)
Sumeini
rock melting
Grt growth
SE11-23 / G2 (in Grt rim)
97.2 ± 0.3 Ma (MSWD = 1.76)
n = 42
Zr = 425 ± 45 ppm
(d)
Sumeini
pre-Grt growth?
SE14-31 / G1 (in Grt core)
100 ± 2 Ma (MSWD = 2.3)
n = 14
Zr = 280 ± 43 ppm
(e)
Sumeini
Grt growth
SE14-31 / G2 (in Grt/Cpx core)
98.0 ± 0.9 Ma (MSWD = 1.8)
n = 35
Zr = 333 ± 40 ppm
(f)
Sumeini
rock melting
Grt growth
SE14-31 / G3 (in Grt / Cpx core)
95.8 ± 0.5 Ma (MSWD = 1.4)
n = 74
Zr = 394 ± 29 ppm
(g)
Sumeini
rock melting
Grt growth
SE14-31 / G4 (in Grt / Cpx / matrix)
95.9 ± 0.5 Ma (MSWD = 1.4)
n = 93
Zr = 442 ± 45 ppm
(h)
Sumeini
Grt breakdown
SE14-31 / G5 (in matrix)
94.9 ± 0.7 Ma (MSWD = 1.4)
n = 35
Zr = 420 ± 67 ppm
(i)
Khubakhib
Grt growth
SE13-123A (in Grt)
96.8 ± 0.4 Ma (MSWD = 1.0)
n = 98
Zr = 451 ± 42 ppm
(j)
Khubakhib
rock melting
SE13-123B (in matrix)
96.6 ± 0.9 Ma (MSWD = 1.8)
n = 57
Zr = 575 ± 37 ppm
(k)
Khubakhib
pre-rock melting
SE13-123G (in Grt)
99.6 ± 1.1 Ma (MSWD = 1.9)
n = 33
Zr = 213 ± 55 ppm
(l)
Sumeini
Grt-free rock
SE14-16B / G1 (in matrix)
97.2 ± 1.4 Ma (MSWD = 2.7)
n = 15
Zr = 195 ± 20 ppm
(m)
Sumeini
Grt-free rock
SE14-16B / G2 (in matrix)
96.3 ± 0.8 Ma (MSWD = 0.97)
n = 36
Zr = 243 ± 46 ppm
(n)
Sumeini
Grt-free rock
SE14-17C / G1 (in matrix)
98.8 ± 1.1 Ma (MSWD = 1.5)
n = 16
Zr = 152 ± 4 ppm
(o)
Sumeini
Grt-free rock
SE14-17C / G2 (in matrix)
97.0 ± 0.6 Ma (MSWD = 1.3)
n = 31
Zr = 210 ± 30 ppm
(p)
Sumeini
Grt-free rock
SE16-20 / G1 (in matrix)
95.2 ± 1.3 Ma (MSWD = 0.91)
n = 9
Zr = 212 ± 18 ppm
(q)
Sumeini
Grt-free rock
SE16-20 / G2 (in matrix)
95.4 ± 0.8 Ma (MSWD = 1.5)
n = 21
Zr = 310 ± 25 ppm
(r)
Sumeini
Grt-free rock
SE16-11 (in matrix)
94.7 ± 0.8 Ma (MSWD = 1.2)
n = 23
Zr = 271 ± 47 ppm
Chondrite-normalized REE
La Ce Pr Nd PaSmEu Gd Tb Dy Ho Er Tm Yb Lu
Zr (ppm)

Figure 5

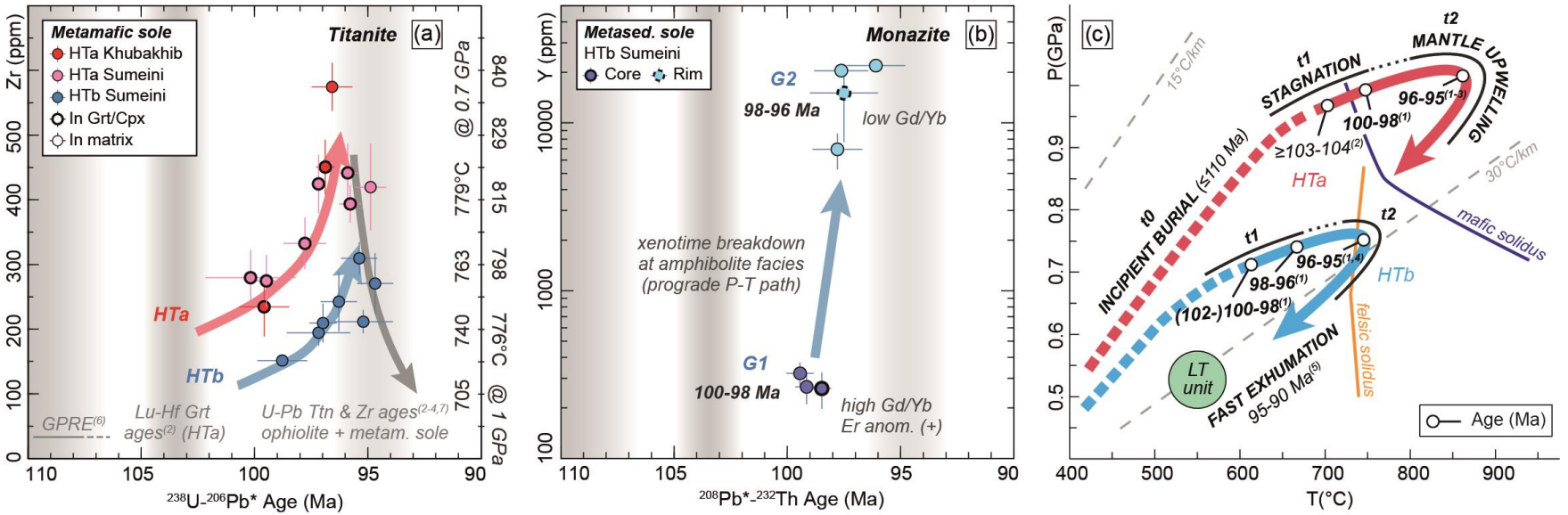

Figure 7

858
859

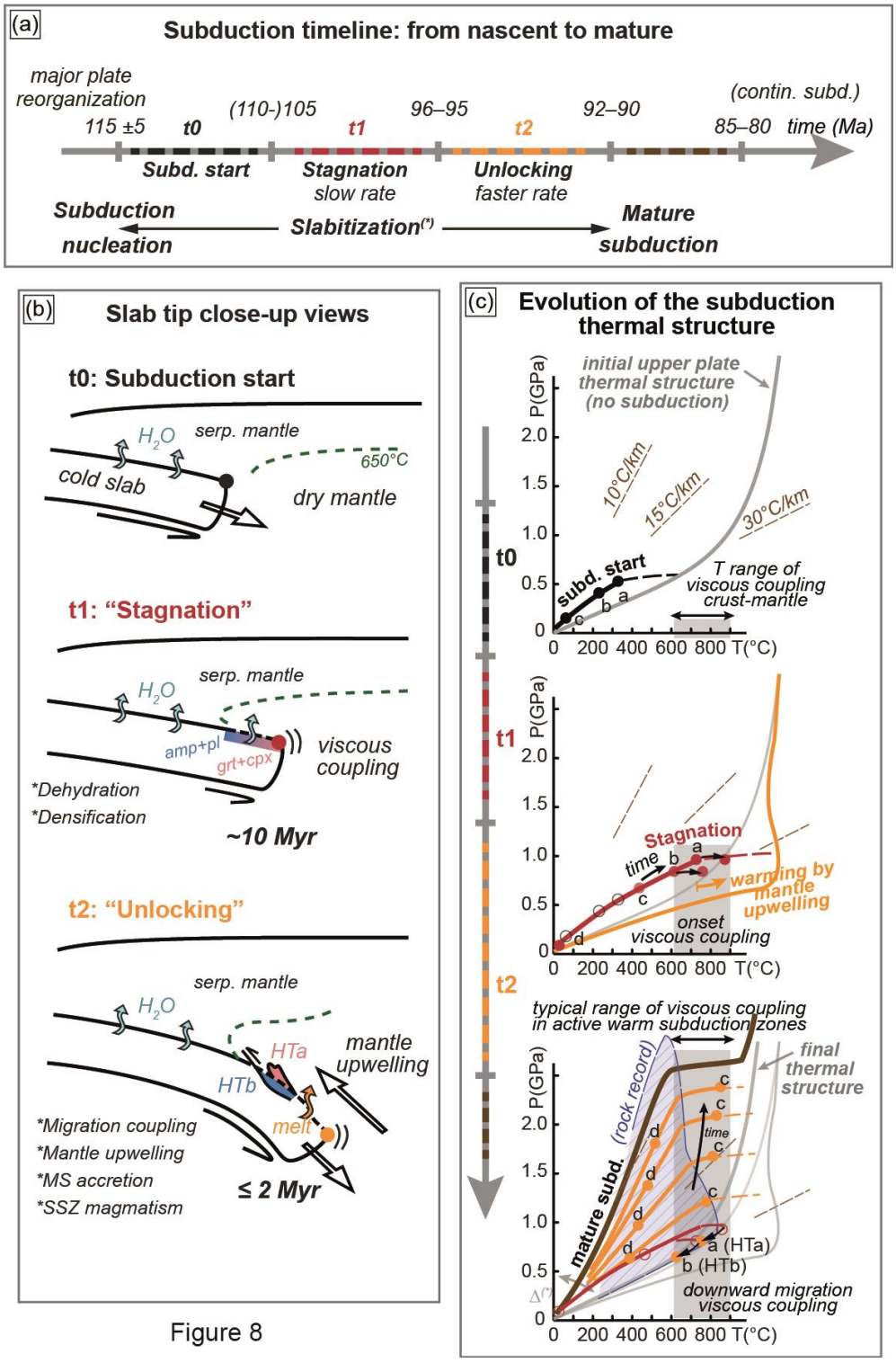
(a)
Subduction timeline: from nascent to mature
major plate reorganization
115 ±5
t0
(110-)105
t1
96–95
t2
92–90
85–80
(contin. subd.)
time (Ma)
Subd. start
Stagnation
slow rate
Unlocking
faster rate
Subduction nucleation
Slabitization(*)
Mature subduction
(b)
Slab tip close-up views
t0: Subduction start
H2O
serp. mantle
650°C
cold slab
dry mantle
t1: "Stagnation"
serp. mantle
H2O
amp+pl
grt+cpx
viscous coupling
*Dehydration
*Densification
~10 Myr
t2: "Unlocking"
serp. mantle
H2O
HTa
HTb
mantle upwelling
melt
*Migration coupling
*Mantle upwelling
*MS accretion
*SSZ magmatism
≤ 2 Myr
(c)
Evolution of the subduction thermal structure
initial upper plate thermal structure (no subduction)
P(GPa)
10°C/km
15°C/km
30°C/km
t0
subd. start
T range of viscous coupling crust-mantle
0 200 400 600 800 T(°C)
t1
Stagnation
time
warming by mantle upwelling
onset viscous coupling
t2
typical range of viscous coupling in active warm subduction zones
final thermal structure
(rock record)
mature subd.
a (HTa)
b (HTb)
downward migration viscous coupling

Figure 8

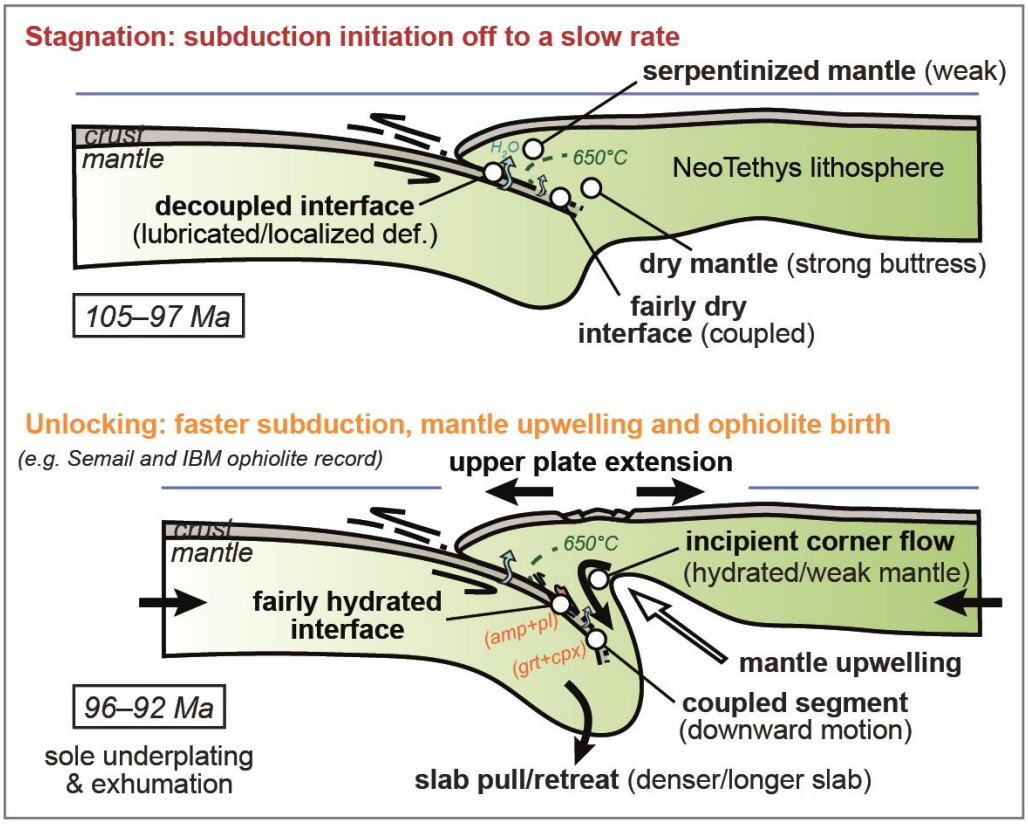
Stagnation: subduction initiation off to a slow rate
serpentinized mantle (weak)
crust
mantle
H2O
650°C
NeoTethys lithosphere
decoupled interface
(lubricated/localized def.)
dry mantle (strong buttress)
105–97 Ma
fairly dry
interface (coupled)
Unlocking: faster subduction, mantle upwelling and ophiolite birth
(e.g. Semail and IBM ophiolite record)
upper plate extension
crust
mantle
650°C
incipient corner flow
(hydrated/weak mantle)
fairly hydrated
interface
(amp+pl)
(grt+cpx)
mantle upwelling
coupled segment
(downward motion)
96–92 Ma
sole underplating
& exhumation
slab pull/retreat (denser/longer slab)

Figure 9

Table 1
U–Th/Pb dates and compositions of titanite and monazite from the Semail metamorphic sole.

Dated mineral	System	Sample	Unit	Locality	Textural position	#(1)	Weighted mean date(2)	W. mean MSWD	Average Zr (ppm)	Average Y (ppm)	Average Gd/Yb
Titanite	U-Pb	SE13-123A	HTa	Khubakhib	in Grt	98	96.9 ± 0.4	1.0	451 ± 42		
		SE13-123B	HTa	Khubakhib	in matrix	57	96.6 ± 0.9	1.8	575 ± 37		
		SE13-123G	HTa	Khubakhib	in Grt	33	99.6 ± 1.1	1.9	235 ± 46		
		SE14-31	HTa	Sumeini	in Grt (G1)	14	100 ± 2	2.3	280 ± 43		
					in Grt and Cpx (G2)	35	98.0 ± 0.9	1.8	333 ± 40		
					in Grt and Cpx (G3)	74	95.8 ± 0.5	1.4	394 ± 29		
					in Grt, Cpx and matrix (G4)	93	95.9 ± 0.5	1.5	425 ± 45		
					in matrix (G5)	35	94.9 ± 0.7	1.4	420 ± 67		
		SE11-23	HTa	Sumeini	in Grt core (G1)	27	99.5 ± 0.7	2.3	275 ± 40		
					in Grt rim (G2)	42	97.2 ± 0.3	1.8	425 ± 45		
Titanite	U-Pb	SE14-16B	HTb	Sumeini	in matrix (G1)	15	97.2 ± 1.4	2.7	195 ± 20		
					in matrix (G2)	36	96.3 ± 0.8	1.0	243 ± 46		
		SE14-17C	HTb	Sumeini	in matrix (G1)	16	98.8 ± 1.1	1.5	152 ± 4		
					in matrix (G2)	31	97.0 ± 0.6	1.3	210 ± 30		
		SE16-11	HTb	Sumeini	in matrix	23	94.7 ± 0.8	1.2	271 ± 47		
		SE16-20	HTb	Sumeini	in matrix (G1)	9	95.2 ± 1.3	0.9	212 ± 18		
					in matrix (G2)	21	95.4 ± 0.8	1.5	310 ± 25		
Monazite	Th-Pb	SE13-123L1	HTb	Sumeini	in matrix Z9 (G2)	7	97.6 ± 1.2	1.0		20417 ± 1420	23 ± 2
		SE13-123L2	HTb	Sumeini	in matrix Z1 (G1)	27	99.2 ± 0.5	1.4		265 ± 55	2180 ± 360
		SE13-123L2	HTb	Sumeini	in matrix Z3 (G2)	7	96.6 ± 1.3	0.6		21867 ± 1686	27 ± 4
		SE13-123L2	HTb	Sumeini	in matrix Z8 (G2)	9	97.8 ± 1.1	1.1		6923 ± 1661	38 ± 4
		SE13-123L2	HTb	Sumeini	in matrix Z9 (G1)	23	99.5 ± 0.6	1.3		320 ± 50	2360 ± 520
		SE13-123L2	HTb	Sumeini	in matrix Z10, grain core (G1)	48	98.5 ± 0.4	1.0		260 ± 60	2670 ± 650
		SE13-123L2	HTb	Sumeini	in matrix Z10, grain rim (G2)	6	97.5 ± 1.5	0.1		15000 ± 7340	41 ± 18

(1) Number of spot analyses; (2) Weighted mean ± 2 SE (Ma); MSWD: Mean Squared Weighted Deviation; Trace element composition ± 1 SE.